

# A novel biomimetic approach to the design of high-performance ceramic–metal composites

Maximilien E. Launey<sup>1</sup>, Etienne Munch<sup>1,†</sup>, Daan Hein Alsem<sup>1,2</sup>,  
Eduardo Saiz<sup>1,‡</sup>, Antoni P. Tomsia<sup>1</sup> and Robert O. Ritchie<sup>1,3,\*</sup>

<sup>1</sup>*Materials Sciences Division, and* <sup>2</sup>*National Center for Electron Microscopy, and*

<sup>3</sup>*Department of Materials Science and Engineering, University of California, Berkeley, CA 94720, USA*

The prospect of extending natural biological design to develop new synthetic ceramic–metal composite materials is examined. Using ice-templating of ceramic suspensions and subsequent metal infiltration, we demonstrate that the concept of ordered hierarchical design can be applied to create fine-scale laminated ceramic–metal (bulk) composites that are inexpensive, lightweight and display exceptional damage-tolerance properties. Specifically, Al<sub>2</sub>O<sub>3</sub>/Al–Si laminates with ceramic contents up to approximately 40 vol% and with lamellae thicknesses down to 10 μm were processed and characterized. These structures achieve an excellent fracture toughness of 40 MPa√m at a tensile strength of approximately 300 MPa. Salient toughening mechanisms are described together with further toughening strategies.

**Keywords:** ceramics; metals; composites; toughness; strength; freeze-casting

## 1. INTRODUCTION

Advances in diverse fields such as aerospace, buildings, transportation and energy require the development of new, high-performance structural materials. In many respects, ceramic–metal composites are ideal candidates. In particular, ceramic-matrix composites (CMCs) are strong, reasonably tough, environmentally stable, lightweight and have the ability to withstand high operating temperatures. Potential applications under development include components for armour, nuclear energy, aerospace and automobiles. Unfortunately, few of these applications have yet to reach commercialization, mostly because of the high cost of these materials and difficulties in their processing (Rosso 2006).

Mechanistically, the concept of ductile-phase toughening of brittle materials (Krstic *et al.* 1981; Sigl *et al.* 1988) has been widely used in composites with different ductile reinforcement morphologies, such as particles, fibres and laminates. However, for the same volume fraction of ductile reinforcing phase, the ductile phase in laminate form has the maximum toughening efficiency, followed (in order of potency) by fibre and particulate morphologies (Rao *et al.* 1992; Soboyejo *et al.* 1996). Specifically, the concept

of laminating various metals and alloys resulting in composites that exploit the unique properties of the constituent materials has been known for a long time (Leichter 1966), and has been embraced as a potential new engineering concept (Lesuer *et al.* 1996). Over the past two decades, a number of diverse brittle ceramics and intermetallics have been toughened with various ductile metal laminates (Dagleish *et al.* 1988, 1989; Bannister & Ashby 1991; Cao & Evans 1991; Odette *et al.* 1992; Shaw *et al.* 1993; Alman *et al.* 1995; Huang & Zhang 1995; Heathcote *et al.* 1996; McNaney *et al.* 1996; Rawers & Perry 1996; Soboyejo *et al.* 1996; Bloyer *et al.* 1998; Enoki *et al.* 1999; Fox & Ghosh 1999; Hwu & Derby 1999*a,b*; Rohatgi *et al.* 2003). A number of these laminate systems were originally conceived and developed with the aim of increasing crack-propagation resistance in brittle components used for high-temperature applications.

Unfortunately, although there are exceptions, strength and toughness tend to be mutually exclusive in these materials and the achievement of optimal mechanical performance in such structural engineering composites is invariably a compromise (Launey & Ritchie 2009). The factors affecting the mechanical response of CMCs have been widely investigated; they include the interfacial adhesion between phases that determines the extent of constraint on the ductile inclusions by the stiff brittle phase (Ashby *et al.* 1989; Cao *et al.* 1989; Deve *et al.* 1990; Deve & Maloney 1991), as well as the effect of reinforcement morphology (shape and size), volume fraction and distribution

\*Author for correspondence (roritchie@lbl.gov).

<sup>†</sup>Present address: Manufacture Française des Pneumatiques Michelin, 63040 Clermont Ferrand, France.

<sup>‡</sup>Present address: Department of Materials, Imperial College London, London SW7 2AZ, UK.

(Rao *et al.* 1992, 1994; Bloyer *et al.* 1998). Consequently, the design of tough materials relies heavily on the control of the material properties and microstructural components at multiple length scales in order to influence the toughening behaviour by optimizing the contributions from both the reinforcing phase and matrix (Becher 1991). One approach is to heed the example of Nature that creates hierarchical hybrid materials such as nacre or bone that, in view of what they are made of, display remarkable properties. These structural biological materials are sophisticated hierarchical composites based on brittle minerals and ductile polymers, which can exhibit mechanical properties that are far beyond those that can be achieved using the same synthetic compounds (Meyers *et al.* 2008a). In particular, the principles of biologically controlled self-assembly in seashells have generated much recent interest (Jackson *et al.* 1988; Kamat *et al.* 2000; Evans *et al.* 2001; Wang *et al.* 2001; Rubner 2003; Mayer 2005); indeed, it has been suggested that their sophisticated structures can offer guidelines for the development of new generations of structural materials (Ortiz & Boyce 2008; Aizenberg & Fratzl 2009).

The creation of artificial Nature-inspired materials with intricate, hierarchical architectures is a challenge that requires both the design of optimum microstructures and the development of fabrication procedures to implement these designs (Espinosa *et al.* 2009). However, conventional processing techniques (e.g. slip/tape-casting combined with hot-pressing, reaction sintering, chemical vapour infiltration, etc.) cannot provide the degree of microstructural control needed to manipulate and optimize the mechanical response of the material. Clegg *et al.* (1990) first developed large-scale nacre-like composites using SiC ceramic tablets coated with graphite to provide weak 'glue' interfaces in order to overcome the brittleness of the ceramic. Although increases in toughness and work of fracture by, respectively, factors of 5 and 100 over monolithic SiC were reported, the toughening achieved by the crack deflection in these macroscopic layered composites was quite limited compared with that seen in the natural composites. Later attempts to develop new nacre-like materials have been usually limited to a few thick (approx. 200  $\mu\text{m}$ ) ceramic layers, approaches that are not appropriate for building synthetic materials with practical sizes. Recently, there have been several outstanding examples of biomimetic organic/inorganic materials fabricated by layer-by-layer deposition (He *et al.* 1997; Kato 2000; Tang *et al.* 2003; Podsiadlo *et al.* 2007; Wei *et al.* 2007; Bonderer *et al.* 2008), self-assembly (Sellinger *et al.* 1998; Hartgerink *et al.* 2001) and thin-film deposition (Chen *et al.* 2007). However, these are invariably limited to thin films or microscopic samples. Largely because of these difficulties in processing, the field of biomimicry has to date generated few new practical *bulk* structural materials.

The key challenge is to find 'top-down' fabrication approaches for the development of metal-ceramic structural materials that both are inexpensive and display unprecedented damage-tolerant (strength and toughness) properties. Recently, a new class of bioinspired ceramic-based materials have been developed

(Deville *et al.* 2006; Munch *et al.* 2008) by controlled freezing of ceramic-based suspensions in water, termed 'ice-templating' or freeze-casting (Deville *et al.* 2006); this technique provides a means to mimic natural structural designs over several length scales. The approach uses the freezing properties of water to make ice/ceramic powder suspensions; when the water is sublimed out, the remaining ceramic scaffold represents the 'negative' of the ice structure. Using this technique, Munch *et al.* (2008) developed a series of bulk ceramic-polymer hybrid materials based on the 'lubricant phase' design concept. The ideal, mimicked from Nature, is to use a hard material (e.g. the ceramic) to provide for strength while using a second (non-load-bearing) ductile phase that acts like a lubricant to permit limited sliding between the ceramic 'bricks' or 'layers' to relieve high stresses (Munch *et al.* 2008; Launey *et al.* 2009). Although different in physical form, the 'lubricant phase' serves the same function as dislocations (plastic deformation) in metals, microcracking in bone or rocks, or crazing in polymers.

In the current study, we use such ice-templating to fabricate bulk ceramic-metal ( $\text{Al}_2\text{O}_3/\text{Al-Si}$ ) layered composites with ceramic layer thicknesses down to 10  $\mu\text{m}$ . This is two orders of magnitude smaller than for ceramic-metal laminates fabricated using conventional processing (e.g. tape- or slip-casting), but still much coarser than the scale of the mineral plates in nacre (which is sub-micrometre). The ice templating process allows control of the lamellar architecture at multiple length scales, resulting in materials that display strength levels comparable to that of  $\text{Al}_2\text{O}_3$  and fracture toughnesses up to 40  $\text{MPa}\sqrt{\text{m}}$ .

## 2. MATERIAL AND METHODS

### 2.1. Processing and sample preparation

Lamellar alumina scaffolds were fabricated in bulk form by freeze-casting (Fukasawa *et al.* 2001; Araki & Halloran 2004; Deville *et al.* 2006; Deville 2008; Waschkies *et al.* 2009) a water-based suspension of sub-micrometre alumina powder (solid content 50 wt%). Sucrose (4 wt%) was added to the suspension in order to ensure the formation of fine ceramic lamellae with a characteristic microscopic roughness (Munch *et al.* 2009). Using controlled directional freezing of the suspension placed on a copper cold finger (figure 1a), large cylindrical porous ceramic scaffolds (50 mm diameter and 50 mm high) were produced with architectures that were templated by the ice crystals (Deville *et al.* 2006, 2007; Munch *et al.* 2008; Launey *et al.* 2009). Directional freezing was first employed to promote the formation of lamellar ice with prescribed dimensions (figure 1b); this then acted as the 'negative' for creation of the layered ceramic scaffolds which were subsequently freeze-dried and sintered (figure 1c). The cooling rates for the cold finger were 1 and  $10^\circ\text{C min}^{-1}$ , which resulted in lamellae thicknesses of approximately 25 and 10  $\mu\text{m}$ , respectively. Patterning of the cold finger combined with vibration was used to align the ceramic lamellae over macroscopic dimensions (Munch *et al.* 2009). This entire process

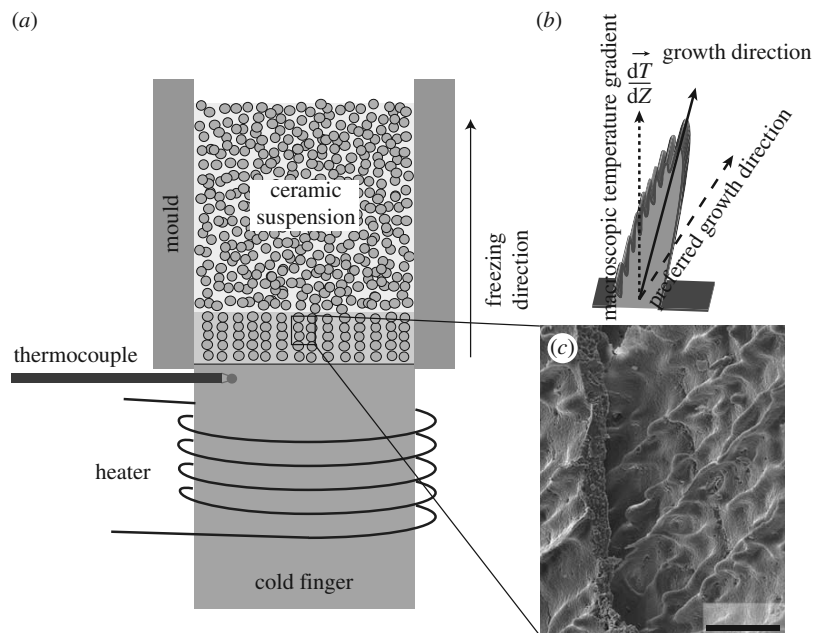


Figure 1. (a) The freeze-casting set-up showing how the ceramic suspension is placed on top of a cold finger that is cooled at a constant rate in order to form a temperature gradient that promotes the formation of lamellar ice. The ice expels the ceramic particles as it grows to leave a layered ceramic structure after water removal. (b) The balance between imposed (parallel to the temperature gradient) and crystallographic-preferred growth directions results in a characteristic dendritic roughness in one of the sides of the growing ice crystals. (c) With sucrose as an additive to the freeze-casting slurry the growing ice crystals develop a characteristic surface topography that translates into a microscopic roughness in the ceramic walls. Scale bar: 25  $\mu\text{m}$ .

led to the formation of bulk ceramic scaffolds—with a ceramic content of approximately 36 vol%—of several centimetres in size formed by macroscopically oriented dense lamellae (figure 1). More information can be found in Launey *et al.* (2009).

The porous ceramics were subsequently infiltrated with molten Al–Si eutectic alloy by fitting the scaffold in an alumina crucible with pieces of Al–Si on top. This alloy was here selected for the infiltration because of its lower melting point and viscosity. The low contact angle of Al–Si on alumina of approximately  $50^\circ$  in vacuum (Saiz & Tomsia 1998) facilitates infiltration at relatively low pressures. The assembly was heated to  $900^\circ\text{C}$  in a  $10^{-4}$  Pa vacuum such that the Al alloy melted and wetted the crucible walls sealing the scaffold from the furnace environment. Thereafter, gaseous argon gas was admitted into the furnace up to a pressure of approximately 70 kPa, and the assembly maintained at a temperature for approximately 5–10 min such that the gas pressure forced the molten alloy into the scaffold porosity. The final composites consisted of fully dense Al–Si-infiltrated  $\text{Al}_2\text{O}_3$  scaffold, where the Si forms needle-like precipitates inside the Al phase (figure 2b).

Rectangular beams for bending tests with the tensile faces parallel to the ceramic layers (crack-arrester orientation) were sectioned from the infiltrated scaffolds using a water-cooled, low-speed diamond saw. The final specimens were 20–25 mm long, 1.5–1.7 mm thick ( $B$ ) and 3.0–3.2 mm wide ( $W$ ). Plane-strain fracture toughness,  $K_{\text{Ic}}$ , and crack resistance-curve ( $R$ -curve) measurements were performed on single-edge notched bend, SE(B), specimens. An initial notch was applied

with a low-speed diamond saw and was subsequently sharpened by repeatedly sliding a razor blade over the saw-cut notch using a custom-made rig, while continually irrigating with a  $1\ \mu\text{m}$  diamond slurry. The final micro-notches had a root radius of approximately 3–5  $\mu\text{m}$ . Sharp cracks with initial crack length  $a \sim 1.6$ – $1.7\ \mu\text{m}$  were generated in general accordance with ASTM standards (E1820-08 2008). The orientation of the notch was such that the nominal crack-growth direction was perpendicular to the ceramic layers.

The damage-tolerance response of these hierarchical materials was also compared with that of the constituent phases— $\text{Al}_2\text{O}_3$  and Al–Si alloy. Dense alumina samples were obtained by slip-casting. The suspensions for slip-casting and freeze-casting used the same starting powders and similar solid contents with identical sintering cycles. Slip-casting was selected to prepare the reference ceramic materials because the ceramic forms through the packing of powders from a liquid suspension, as in freeze-casting. The binary Al–12.6 wt%Si eutectic alloy was processed by vacuum arc-melting of ultrasonically cleansed Al and Si elements of high purity ( $>99.99\%$ ).

Alumina SE(B) specimens (24 mm long, 6 mm wide and 2.4–2.5 mm thick) were fatigue pre-cracked using a half-chevron starter notch in addition to a Vickers hardness indent placed at the notch tip in order to facilitate crack initiation. Prior to  $R$ -curve testing, a SE(B) specimen of Al–Si (50 mm long, 10 mm wide and 9.2 mm thick) was fatigue pre-cracked in three-point bending on a servo-hydraulic mechanical testing machine using a bend fixture. A pre-crack was grown, in accordance with ASTM standards (E1820-08 2008) from a machined notch, of length  $0.4W$ , to a final

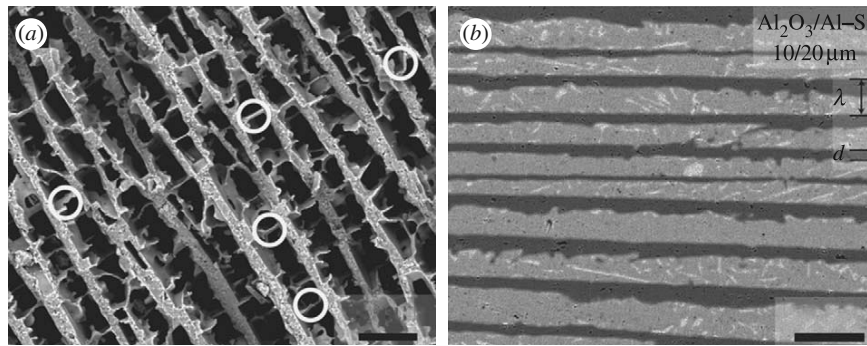


Figure 2. (a) Porous scaffolds of practical dimensions obtained by freeze-casting of ceramic suspensions. The process results in the formation of ceramic bridges—some of them are highlighted by the circles—between lamellae owing to the trapping of ceramic particles by the growing ice. (b) Backscattered electron micrograph of a 10/20 structure (the dark phase is the ceramic, the lighter phase is the metal and the bright needle-like regions are silicon precipitates). The control of the processing conditions leads to macroscopic samples that exhibit lamellar structures oriented over several centimetres followed by metal (Al–Si eutectic) infiltration.  $\lambda$  represents the microstructural wavelength, and  $d$  the thickness of the  $\text{Al}_2\text{O}_3$  lamellae. Scale bar: 50  $\mu\text{m}$ .

crack length of  $0.5W$ . Cycling was performed at 25 Hz with a constant load ratio (ratio of minimum to maximum load,  $R = K_{\min}/K_{\max}$ ) of 0.1; the final maximum stress intensity,  $K_{\max}$ , was 4.4  $\text{MPa}\sqrt{\text{m}}$ . Prior to testing, all specimens were polished on both faces down to a 1  $\mu\text{m}$  finish using diamond suspensions.

As a basis for comparison, small beams (20 mm long, 2.3–2.4 mm wide and 1.2–1.4 mm thick) were prepared from the nacreous layer of a red abalone shell (*Haliotis rufescens*). Samples were kept immersed in water to keep them hydrated until testing. More information is provided in Launey et al. (2009).

## 2.2. Microstructural characterization

To characterize the nano/microstructure, and in particular the ceramic–metal interfaces, samples were prepared for high-resolution scanning transmission electron microscopy (STEM) imaging and electron energy-loss spectroscopy (EELS) in an aberration-corrected VG HB 501 microscope (with a field-emission gun at 100 kV). First, 3 mm disc samples were mechanically polished and dimpled down to about 30  $\mu\text{m}$  thickness, after which electron-transparent windows (down to approx. 100 nm thickness) were created by local focused ion beam (FIB) thinning (FEI Strata 235 Dual Beam FIB) of a disc that was cut in half and placed upright with the straight side facing the ion beam. A protective platinum layer was deposited on the surface prior to final thinning with the ion beam.

## 2.3. Mechanical characterization

**2.3.1. Strength and  $K_{Ic}$  measurements.** Three-point bend tests were performed to generate quantitative stress–strain curves and to measure the plane-strain fracture toughness,  $K_{Ic}$ . The strength tests were performed on unnotched bend specimens using a support span  $S$  of 12.5 mm and a displacement rate of 1  $\mu\text{m s}^{-1}$  in general accordance with ASTM standards (E1820-08 2008). The toughness measurements were performed on SE(B) specimens, also loaded with  $S = 12.5$  mm. Values were determined by monotonically loading the specimens to failure at a constant displacement rate of 1  $\mu\text{m s}^{-1}$ .

All toughness tests satisfied the plane-strain and small-scale yielding requirements for valid  $K_{Ic}$  measurement, as per ASTM standards (E1820-08 2008); all the values presented represent at least an average of three measurements per configuration ( $N \geq 3$ ).

**2.3.2. Fracture toughness  $J$ – $R$  curve measurements.** In order to capture both intrinsic (plasticity) and extrinsic (crack-tip shielding) toughening mechanisms acting in these materials, nonlinear-elastic fracture mechanics methods were performed using SE(B) specimens in the crack-arrester orientation.  $R$ -curves were measured in ambient air to evaluate the fracture resistance in terms of the  $J$ -integral as a function of crack extension,  $\Delta a$ , under a monotonically increasing driving force. Tests were conducted in three-point bending with a span ( $S = 12.5$  mm) to width ( $W \sim 3$  mm) ratio of approximately 4, in accordance with ASTM standards (E1820-08 2008). The specimens were loaded in displacement control in a servo-hydraulic testing machine with a loading rate of approximately 0.015  $\text{mm s}^{-1}$  until the onset of cracking, which was determined by nonlinearity in the load–displacement curve. To monitor subsequent subcritical crack growth, at this point during the loading, the sample was periodically unloaded (by approx. 10–20% of the peak load) to record the elastic load-line compliance using a linear variable differential transformer (LVDT) mounted on the load frame. After each increment, a measurement of the compliance was made during unloading after the specimens had been held for 30 s to allow the crack extension to stabilize. This process was repeated at regular intervals until the end of the test, at which point the compliance and loading data were analysed to determine  $J$ -integral as a function of  $\Delta a$ . Crack lengths,  $a$ , were calculated from the compliance data obtained during the test using compliance expression of a three-point bend specimen at load line (Haggag & Underwood 1984):

$$\frac{a}{W} = 0.997 - 3.58U - 1.51U^2 - 110U^3 + 1232U^4 - 4400U^5, \quad (2.1)$$

where  $U$  is a fitting function, written as

$$U = \frac{1}{\sqrt{FC} + 1}. \quad (2.2)$$

Here  $C$  is the sample compliance, and  $F$  is a calibration factor, taken to be that which gives the best agreement between the initial compliance and crack length at the beginning of the test. The same procedure was used for the Al–Si specimen.

In addition,  $R$ -curves were measured *in situ* in a scanning electron microscope (SEM) using a Gatan Microtest three-point bending stage. Crack extension was monitored directly in backscattered electron mode at a pressure of 35 Pa and a 30 kV excitation voltage.

For  $R$ -curve determination, small-scale bridging conditions were assumed, where the size of the zone of crack bridges behind the crack tip remained small compared with the in-plane test specimen dimensions. As noted above, the use of the  $J$ -integral as the driving force for crack initiation and growth was employed to capture the contribution from inelastic deformation in the evaluation of toughness. The stress intensity at each measured crack length was calculated by measuring the nonlinear strain-energy release rate,  $J$ . The value of  $J$  was calculated from the applied load and instantaneous crack length according to ASTM standards (E1820-08 2008), and was decomposed into its elastic and plastic contributions:

$$J = J_{\text{el}} + J_{\text{pl}}. \quad (2.3)$$

The elastic contribution  $J_{\text{el}}$  is based on linear-elastic fracture mechanics:

$$J_{\text{el}} = \frac{K_{\text{I}}^2}{E'}, \quad (2.4)$$

where  $K_{\text{I}}$  is the mode I stress-intensity factor, and with  $E' = E/(1 - \nu^2)$  in plane strain ( $\nu$  is Poisson's ratio and  $E$  is Young's modulus). Using the load-line displacements, the plastic component  $J_{\text{pl}}$  for a stationary crack in bending is given by

$$J_{\text{pl}} = \frac{1.9A_{\text{pl}}}{Bb}, \quad (2.5)$$

where  $A_{\text{pl}}$  is the plastic area under force versus displacement curve and  $b$  the uncracked ligament length ( $W - a$ ).

Equivalent  $K$ -based fracture toughness values were also estimated from the  $J$  measurements using the standard  $J$ - $K$  equivalence for nominal mode I fracture, specifically that  $K_{\text{J}} = (J.E')^{1/2}$ . These calculations require knowledge of the Young's modulus  $E$ . The structure of the lamellar hybrid composites is clearly directional; properties are orthotropic, with values of  $E$  lying between the upper and lower bound of the 'rule of mixtures', as defined by the Voigt and Reuss models, respectively. Measurements using three-point bend tests showed that the elastic modulus values fell approximately at the midpoint between these upper and lower bounds. Using  $E$  values for Al–Si of 79 GPa and for  $\text{Al}_2\text{O}_3$  of 300 GPa, the elastic modulus for the lamellar hybrid structures at 36 vol% ceramic content was calculated to be 133 GPa in the direction perpendicular to the ceramic layers. These values were

confirmed experimentally by contact ultrasonic measurements using a pulse-echo overlap technique with MHz shear and longitudinal piezoelectric transducers, and a pulser/receiver to measure the shear and longitudinal wave speeds at room temperature. Note that a relatively small error in the value of  $E$  would have a limited impact on the computed  $K_{\text{J}}$  toughness; specifically, a  $\pm 20$  per cent error in  $E$  results in a  $\pm 10$  per cent error in  $K_{\text{J}}$ .

### 3. RESULTS

#### 3.1. Microstructure

The controlled directional freezing of water-based ceramic suspensions combined with liquid metal infiltration was used to create laminated metal–ceramic hybrid materials with ceramic layers of homogeneous thickness running continuously from the bottom to the top of the sample (figure 2a). A key aspect of the process is to align the layers over macroscopic dimensions rather than in randomly oriented microscopic domains (Munch *et al.* 2009; Ziegler *et al.* 2009). This was achieved here by patterning the cold finger together with applying vibration during freezing. In this way ceramic lamellae with grain sizes of the order of 1  $\mu\text{m}$  were fully aligned on centimetre-sized samples.

A key characteristic of the freeze-casting process is the ability to manipulate the material structure at multiple dimensions. It has been shown that the roughness of the nacre tablets and the mineral bridges between them play a critical role in controlling shear at the organic–inorganic interface during loading as the sliding of adjacent tiles requires the breaking of bridges and together with the roughness they provide additional frictional resistance (Evans *et al.* 2001; Meyers *et al.* 2008b; Espinosa *et al.* 2009). Different additives can be used to control the microstructure of the ice crystals in the suspensions that will translate into characteristic roughness for the ceramic lamellae. The additives modify the interfacial tensions, the degree of supercooling ahead of the ice front and the viscosity and the phase diagram of the solvent, promoting, for example, the formation of fugitive phases that are eliminated during sintering. They also affect interparticle interactions that in turn determine the formation of bridges through particle trapping by the growing ice front. In the present study, the use of sucrose resulted in the formation of microscopic roughness (figure 1c) characterized by relatively smooth dendritic-like features, 1–5  $\mu\text{m}$  high, running in the direction of solidification in one of the lamellae sides (Deville *et al.* 2007; Munch *et al.* 2009) and the formation of thin ( $\leq 1 \mu\text{m}$ ) ceramic bridges (figure 1a) after sintering.

The microstructural wavelength,  $\lambda$ , and the ceramic lamellae thickness,  $d$  (figure 2b) are primarily a function of the ice-front velocity and to a lesser extent the ceramic particle size (Deville *et al.* 2007; Deville 2008). As our objective was to mimic the nacre structure and fabricate samples with larger ceramic contents, the solid content of the suspensions was maximized to the order of 50 wt% (approx. 20 vol%). The porosity of the resulting scaffolds after sintering was

approximately 64 vol% and the  $\text{Al}_2\text{O}_3/\text{Al-Si}$  lamellae thickness,  $d$ , was approximately 10/20 and 25/50  $\mu\text{m}$  for cold finger cooling rates of 10 and  $1^\circ\text{C min}^{-1}$ , respectively. Finer  $\text{Al}_2\text{O}_3$  lamellae of approximately 5  $\mu\text{m}$  can be obtained by faster ice growth (Deville *et al.* 2007). However, these finer scaffolds could not be infiltrated under the present conditions. Although the contact angle of Al–Si alloys on alumina is relatively low (approx.  $50^\circ$ ), several factors impede spontaneous infiltration; these include the roughness of the lamellae (Trumble 1998) and the presence of an oxide layer on the metal surface. Consequently, an additional pressure, which is inversely proportional to the pore size (Garcia-Cordovilla *et al.* 1999), is required to break the oxide layer and promote infiltration. At present, our experimental set-up cannot reach the pressures needed to infiltrate the finer microstructures. Furthermore, it is apparent from high-resolution STEM (figure 3) that a calcium-rich layer forms at the  $\text{Al}_2\text{O}_3/\text{Al-Si}$  interface, as well as on the  $\text{Al}_2\text{O}_3$  grain boundaries. Segregation of calcium at aluminium–alumina interfaces has been previously observed (Kaplan *et al.* 1995; Kaplan 1998). Calcium is a common impurity in many commercial powders and it is known to cause exaggerated grain growth during sintering of  $\text{Al}_2\text{O}_3$ , and may affect infiltration.

### 3.2. Strength and fracture toughness

Bending stress–strain curves for the  $\text{Al}_2\text{O}_3/\text{Al-Si}$  hybrid composites, namely the 10/20 and 25/50 (numbers corresponding to the  $\text{Al}_2\text{O}_3$  and Al–Si lamellae thicknesses in micrometres, respectively), indicated that decreasing the thickness of the ceramic has a minimal effect on the flexural (ultimate) strengths, as the latter are comparable to that of pure  $\text{Al}_2\text{O}_3$ , with average values of  $328 \pm 11$  MPa and  $352 \pm 3$  MPa for the 10/20 and 25/50 composites, respectively (figure 4b). By comparison, the flexural strengths of pure  $\text{Al}_2\text{O}_3$  and Al–Si were found to be  $325 \pm 20$  MPa and  $302 \pm 10$  MPa. However, the main distinction is that the coarser structure shows approximately 1 per cent inelastic deformation prior to failure, while plasticity is suppressed in the finer composite that does not exhibit macroscopic plastic deformation prior to failure (figure 4a).

Values of the fracture toughness for crack initiation,  $K_{\text{Ic}}$ , were  $8.3 \pm 0.3$  MPa $\sqrt{\text{m}}$  and  $7.2 \pm 0.3$  MPa $\sqrt{\text{m}}$  for the 10/20 and 25/50 composites, respectively (figure 4b). Refinement of the lamellae size slightly improved the  $K_{\text{Ic}}$  of lamellar structures, which is consistent with our investigations on organic–inorganic hybrid composites (Launey *et al.* 2009); it implies that flaws in the material control the initiation toughness, with the thicker lamellae representing a larger statistical sampling volume with a higher probability of finding a large flaw.

Full  $K_{\text{R}}(\Delta a)$  resistance curves of the composites are shown in figure 4c and are expressed in terms of the equivalent stress intensity,  $K_{\text{J}}$ , as a function of crack extension,  $\Delta a$ . The hybrid composites both display  $R$ -curve behaviour which demonstrates that these materials derive most of their resistance to fracture during crack growth, and not during crack initiation.

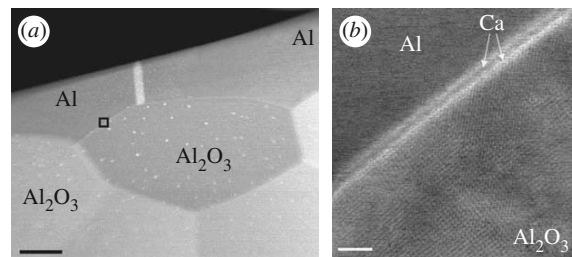


Figure 3. High-angle annular dark field STEM imaging of an aluminium–alumina interface in the composite (there are no silicon precipitates in the field of view). (a) Lower magnification overview of the interface showing the  $\text{Al}_2\text{O}_3$  grain structure, as well as brighter Z-contrast around the  $\text{Al}_2\text{O}_3$  grains. Note that the small speckles are platinum debris resulting from the FIB milling. The bright vertical band in the Al, although not characterized in detail, is associated with a boundary between two aluminium grains. Scale bar: 500 nm. (b) High-resolution STEM image of the interface showing more clearly several atomic layers of bright Z-contrast at the Al– $\text{Al}_2\text{O}_3$  interface. EELS shows these bright atomic layers to contain calcium, indicating that these interfaces are decorated with calcium impurities. Scale bar: 5 nm.

This is no surprise as the extrinsic crack-tip shielding mechanisms, which include crack bridging via ductile reinforcements, primarily act behind the crack tip and locally screen the crack from the applied (far-field) driving force (Ritchie 1988; Sigl *et al.* 1988; Evans 1990). The additional energy required to fracture the bridging ligaments is typically exhibited in the form of resistance-curve ( $R$ -curve) behaviour, where the crack-growth toughness increases with crack extension, commensurate with the development of a bridging zone in the crack wake (figure 5a,b). In fact,  $R$ -curve behaviour has been widely reported in other laminated metal–ceramic systems (Shaw *et al.* 1993; Rao *et al.* 1994; Soboyejo *et al.* 1996; Bloyer *et al.* 1998; Hwu & Derby 1999b; Rohatgi *et al.* 2003; Mekky & Nicholson 2006).

Specifically, the 25/50 hybrid composites reach a (steady-state) fracture toughness  $K_{\text{Jc}}$  of approximately 40 MPa $\sqrt{\text{m}}$  ( $J_{\text{c}}$  approx.  $11 \text{ kJ m}^{-2}$ ) after 1 mm of crack extension (figure 4c). This leads to toughness values that are above the rule of mixtures of the components (figure 4d). However, the refined structure (10/20) shows significantly less stable growth before critical fracture, and a maximum toughness  $K_{\text{Jc}}$  of 22 MPa $\sqrt{\text{m}}$  ( $J_{\text{c}}$  approx.  $3 \text{ kJ m}^{-2}$ ) after approximately 500  $\mu\text{m}$  of crack extension. The lower toughness can be explained here by the ‘loss’ of ductility, as seen in figure 4a.

The fact that the  $R$ -curves reach a steady-state plateau (figure 4c) is an indicator that the small-scale bridging (SSB) conditions prevailed. The bridging phenomenon can be divided into SSB and large-scale bridging (LSB) depending upon whether the size of the bridging zone is, respectively, small or comparable to the crack length and in-plane specimen dimensions. SSB ensures that the critical toughness,  $K_{\text{Jc}}$ , is independent of crack length and specimen geometry. According to active ASTM standards (E1820-08 2008), the measurement capacity of a given sample is limited by its maximum  $J$ -integral capacity,  $J_{\text{max}}$ , and its maximum crack extension capacity,  $\Delta a_{\text{max}}$ .  $J_{\text{max}}$  is given by

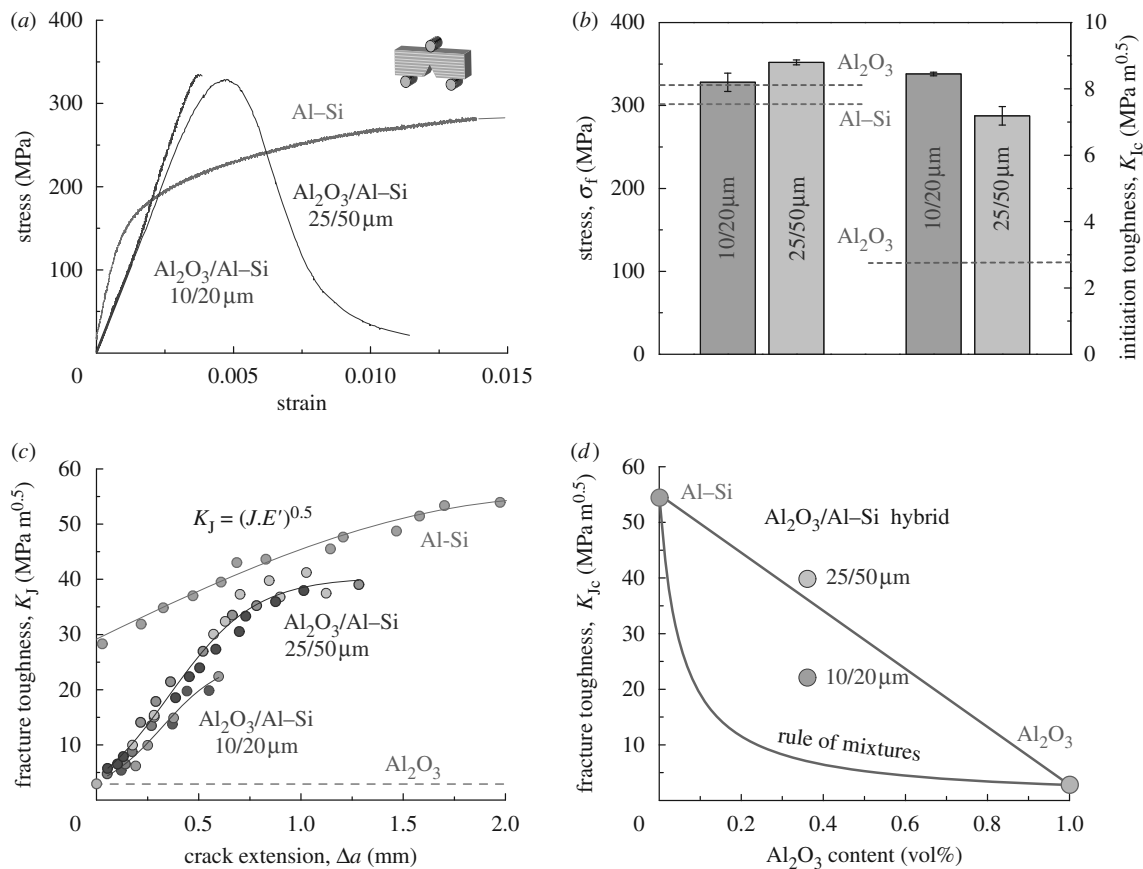


Figure 4. (a) Single-edge notched bending stress–strain curves for the  $\text{Al}_2\text{O}_3/\text{Al-Si}$  hybrid materials compared with dense  $\text{Al-Si}$ . The 25/50 lamellar composites show ductile behaviour with more than 1 per cent inelastic deformation prior to failure, while the finer structure (10/20) displays a rather brittle behaviour with essentially no macroscopic ductility. (b) Strength and crack-initiation toughness,  $K_{Jc}$ , of the lamellar composites. (c) Crack-resistance curves ( $R$ -curves) showing resistance to fracture in terms of the stress intensity,  $K_J$ , as a function of crack extension,  $\Delta a$ , for the hybrid composite as well as for dense  $\text{Al-Si}$  and  $\text{Al}_2\text{O}_3$ . The fracture toughness,  $K_J$ , is back-calculated from the  $J$  measurements using the  $J$ - $K$  equivalence for mode I fracture (see text). (d) Crack-growth toughness of the dense components, along with that from the rule of mixtures, and  $K_{Jc}$  measurements for  $\text{Al}_2\text{O}_3/\text{Al-Si}$  composites. The upper and lower bounds of the rule of mixtures were defined by the Voigt and Reuss models, respectively.

the smaller of  $b\sigma_y/10$  or  $B\sigma_y/10$ ; similarly,  $\Delta a_{\text{max}}$  is given by  $0.25b$ . The  $R$ -curve is therefore defined as the data in a region bounded by these  $J_{\text{max}}$  and  $\Delta a_{\text{max}}$  limits (Launey *et al.* 2009); therefore, the maximum measurement capacity of the specimens are  $J_{\text{max}} = 45 \text{ kJ m}^{-2}$  (with  $b, B = 1.5 \text{ mm}$ ) and  $\Delta a_{\text{max}} = 0.375 \text{ mm}$  (with  $b = 1.5 \text{ mm}$ ). The ASTM standards provide a somewhat arbitrary conservative limit. However, a critical toughness,  $J_c$ , can be defined here before the measurement becomes geometry-dependent owing to LSB. This criterion yields  $J$ -integral values that are slightly above the maximum crack extension,  $\Delta a_{\text{max}}$ , but have a clear physical meaning. Most importantly, the conditions for  $J$ -dominance were met in all the tests such that  $b, B \gg 10 (J_c/\sigma_y)$ . This latter criterion ensures that the  $J$ -integral (and subsequently  $K$ ) values represent valid fracture toughness values.

### 3.3. Crack-growth observations

The salient sources of toughening in the ceramic–metal hybrid composites were identified by performing

additional fracture toughness tests *in situ* in the SEM. This technique provides the opportunity to measure quantitatively the  $R$ -curve, while simultaneously monitoring the evolution of damage mechanisms ahead of the growing crack and toughening mechanisms that result in the wake; furthermore, how these mechanisms relate to the composite architecture can be imaged in real time (figures 5 and 6). In the coarser composite, multiple cracks formed within the  $\text{Al}_2\text{O}_3$  layers after initial renucleation from the pre-crack (figure 5a). In fact, lateral spreading of multiple cracks within the same brittle layer occurred in preference to forward progression of the main crack. In contrast, fracture in the finer-scale 10/20 laminate can be characterized as single (dominant) fracture, where the crack propagates by renucleation in successive ceramic layers following an approximately co-planar path (figure 5b). The ‘multiple cracking’ fracture mode occurring in the 25/50 composite, with its greater distribution of damage over millimetre scales (figure 5a) and higher energy absorption, leads to significantly higher toughness (figure 4c). As discussed in the next section, the

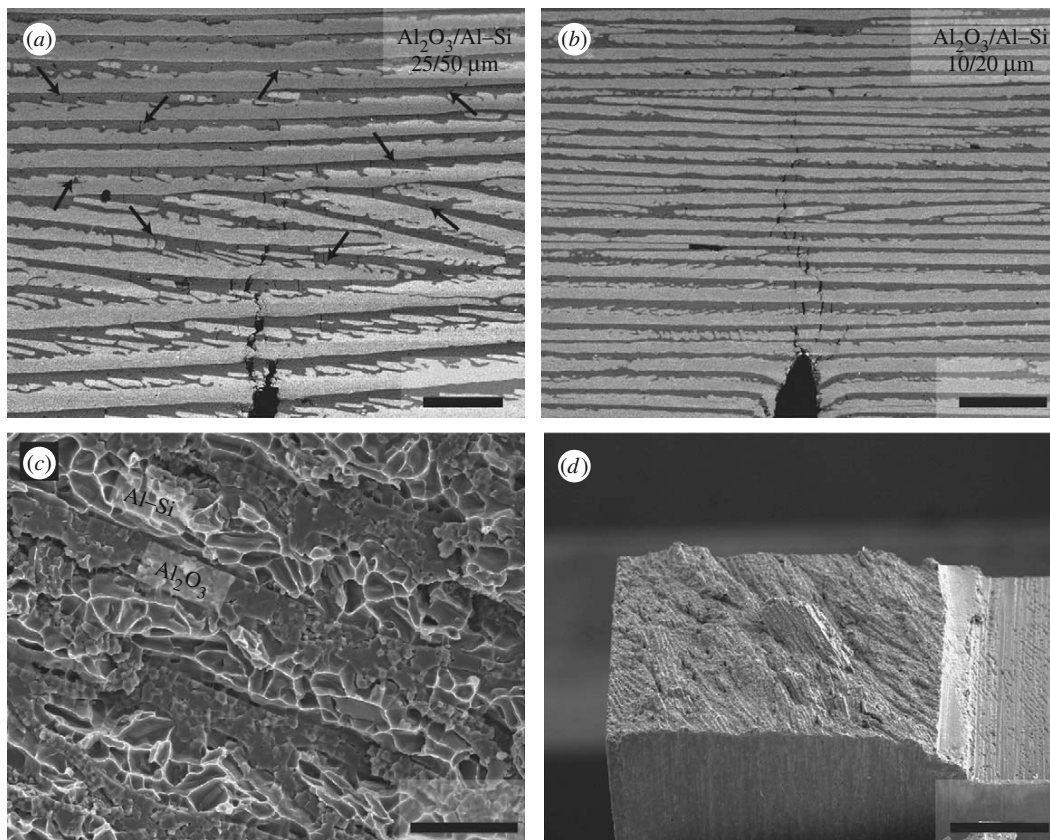


Figure 5. (a,b) Backscattered electron images of stable crack growth during *in situ* *R*-curve testing show (a) multiple cracking fracture mode in the coarser structure and (b) dominant single cracking in the finer structure. Scale bar: (a,b) 200  $\mu\text{m}$ . The arrows in (a) indicate the presence of the microcracks. Lateral microcracks might be observed in (b); however, the volume of material involved in multiple cracking is negligible compared with (a). (c,d) Typical secondary electron micrographs of the fracture surfaces show relatively flat surfaces in both structures indicative of no delamination owing to strong bonding. Scale bar: (c) 25  $\mu\text{m}$ ; (d) 500  $\mu\text{m}$ .

transition from multiple to single dominant cracking is controlled by the flow properties, the scale of the microstructure and the properties of the ceramic-metal interface (Deve *et al.* 1990; Deve & Maloney 1991; Shaw *et al.* 1993). Observation of the fracture surfaces (figure 4c,d) indicated that no interfacial debonding occurred in any of the composites, during either crack renucleation or subsequent fracture, despite extensive plastic stretching of the metal layers (figure 6c); this implies strong bonding between  $\text{Al}_2\text{O}_3$  and Al-Si. Ductile ligaments bridge the advancing crack (figure 6a), and stretch (figure 6c) as the crack opens until they fracture or decohere; such plastic stretching contributes to the overall toughness. In addition, significant crack blunting is observed (figure 6a) which occurs when the crack encounters a ruptured region and is consequently blunted; further crack-growth requires renucleation, i.e. a significant amount of energy absorption, resulting in an increase in toughness.

#### 4. DISCUSSION

The *in situ* analysis of crack growth clearly shows how control of the structural architecture at several length scales permits the generation of multiple toughening

mechanisms operating over a large range of dimensions. Toughening in materials is broadly divided into two categories—*intrinsic* and *extrinsic* (Ritchie 1988). *Intrinsic* toughening mechanisms increase the inherent microstructural resistance to crack initiation and growth, as exemplified by the role of plasticity ahead of the crack tip in metals. Conversely, *extrinsic* toughening involves deformation and microstructural mechanisms that act primarily behind the crack tip to inhibit crack growth by effectively reducing (‘shielding’) the crack-driving force actually experienced at the crack tip. The toughening mechanisms identified in our  $\text{Al}_2\text{O}_3/\text{Al-Si}$  hybrid composites are primarily of the *extrinsic* type, as in most brittle-matrix laminates (Lesuer *et al.* 1996). The most prominent toughening mechanism here is ductile-ligament bridging (figure 6a), where unbroken ductile ligaments span the wake of the crack (Sigl *et al.* 1988). Further crack growth requires stretching of the bridging ligaments (figure 6c) which must have sufficient ductility to avoid fracture at or ahead of the crack tip. Stretching is further impeded by the controlled lamellae roughness and the presence of ceramic bridges (figures 1c and 2a). These mechanisms result in the typical *R*-curve behaviour and are dependent upon the volume fraction of the ductile phase (Evans 1990). Crack blunting in Al-Si was also identified as an important toughening

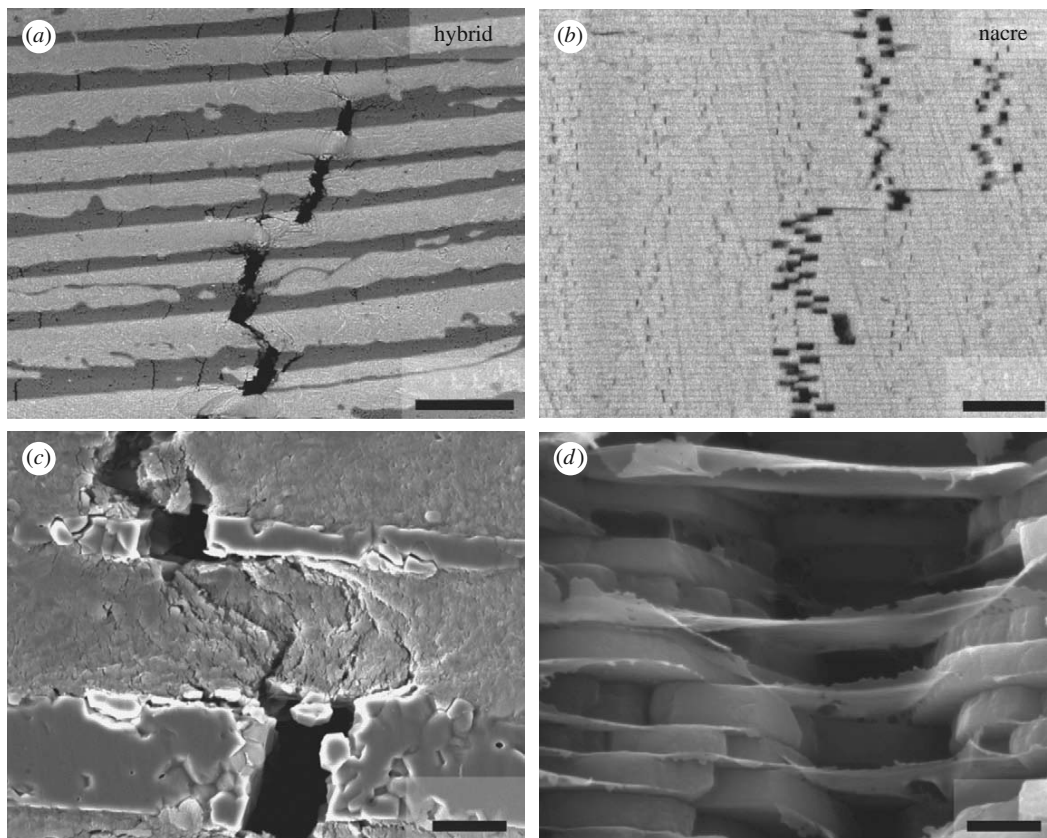


Figure 6. Comparison of the mechanisms of damage and toughening in synthetic and natural materials, showing (a,b) backscattered and (c,d) secondary electron images of stable crack growth in (a,c) the  $\text{Al}_2\text{O}_3/\text{Al-Si}$  hybrid composites and (b,d) hydrated nacre (red abalone shell) showing some similarities in their toughening mechanisms. (a,c) Damage spreading, ductile-ligament bridging, ductile stretching and tearing are some of the identified toughening mechanisms akin to those observed in (b,d) nacre. Note that the production of such lamellar structures is not enough to guarantee nacre-like behaviour; material design must exhibit characteristic structural features such as refined lamellae or brick-like structures with appropriate interface adhesion to permit limiting interlamellar slip or 'lubrication'. Scale bar: (a) 100  $\mu\text{m}$ ; (b) 5  $\mu\text{m}$ ; (c) 10  $\mu\text{m}$ ; (d) 1  $\mu\text{m}$ . Image in (b) from Espinosa *et al.* (2009).

mechanism that acts to lower crack-tip stresses; in fact, it has been observed that an increase in layer thickness results in an increased degree of blunting, which is consistent with previous observations (Kruzic *et al.* 2004).

Most importantly, the resulting fracture toughness of our composites was highly dependent on the crack-propagation mode. Damage develops either as a dominant (single) crack, or as periodic (multiple) cracks, depending on the layer thickness (figure 5a,b). As in nacre, multiple cracking is more desirable as it leads to superior toughness (figure 6b,d). The transition from single to multiple cracking is controlled by the flow properties of the metal, the scale of the microstructure and the properties of the metal–ceramic interface (Deve *et al.* 1990; Deve & Maloney 1991; Shaw *et al.* 1993). Specifically, it has been suggested that this transition is a function of the ratio of the metal layer thickness,  $t_m$ , to the ceramic layer thickness,  $t_c$ . For a given combination of metal and ceramic, there is a critical thickness ratio  $(t_m/t_c)_{\text{crit}}$ , above which multiple cracking prevails. This critical thickness ratio decreases with the effective (constrained) metal yield stress,  $\sigma_m$ , as a fraction of ceramic strength,  $\sigma_c$ , and with decreasing metal–ceramic elastic modulus ratio,  $E_m/E_c$  (Shaw *et al.* 1993; Huang *et al.* 1994; Huang & Zhang 1995;

Shaw *et al.* 1996). Single fracture occurs if the maximum stress in the ceramic layer ahead of the initial crack,  $\sigma_{\text{max}}$ , exceeds the ceramic fracture strength,  $\sigma_c$ , before the stress in the ceramic layers in the wake,  $\sigma_o$ , exceeds this level (Huang & Zhang 1995), such that  $\sigma_{\text{max}} = \sigma_c > \sigma_o$  for multiple cracking, and  $\sigma_o = \sigma_c > \sigma_{\text{max}}$  for single cracking. This model (Huang & Zhang 1995), which is based on nonlinear-elastic fracture mechanics and fibre bridging, predicts that multiple cracking is ensured if the metal layer thickness is 2.5 times larger than the ceramic layer thickness, regardless of the ceramic–metal properties. In our hybrid composites,  $t_m/t_c < 2.5$  (approx. 2) implying that the cracking mode becomes dependent on the constrained metal yield stress,  $\sigma_m$ . The effect of metal plasticity was in fact found to be important, especially when low yield strength metals, such as aluminium, are used in the laminate (Hwu & Derby 1999a). Additional constraint of the plastic zone may occur when plasticity extends across the thickness of the metal layer, impinging on the ceramic. Constraint through the ceramic layer is significantly affected by the metal layer thickness; in fact, theoretical studies have shown that the plastic-zone size, crack-tip opening displacement (CTOD) and the stress state near a crack tip are all affected by variations

in the layer thickness (Varias *et al.* 1991). In accordance with previously studied  $\text{Al}_2\text{O}_3/\text{Al}$  laminates, it appears that, as the layer thickness of metal increases, the stresses in the crack wake increase, whereas the stresses in the intact layer ahead of the crack tip decrease (Shaw *et al.* 1993). This trend leads to a transition in cracking mechanism with increasing layer thickness of metal, whenever the metal layers have sufficiently high yield strength. Specifically, for lowest metal layer thickness, mode I extension of a primary crack takes place, whereas for the coarser laminates, periodic multiple cracking occurs.

Crack deflection via layer delamination is a very effective toughening mechanism in ceramic–metal composites although it may compromise strength (Evans 1990). However, higher toughness is achieved by extensive debonding when the reinforcement exhibits high work hardening. Conversely, debonding is not beneficial when the reinforcement exhibits low intrinsic ductility owing to an absence of work hardening (Deve *et al.* 1990). The use of interfacial segregants on metal–oxide interfaces (Hong *et al.* 1995; Gaudette *et al.* 1997; Saiz *et al.* 2000), or inert oxide coatings emplaced between the reinforcement and the matrix (Deve & Maloney 1991) can induce extensive debonding, leading to enhanced values of the toughness. However, aluminium–alumina interfaces formed in the liquid state are usually stronger than those formed in the solid state (Saiz *et al.* 2003) and no such delamination was observed in our composites (figure 5c).

In any event, it is clear that the fracture toughness of the hybrid composite is dictated by the relatively thick (soft) metallic phase which plays a structural, load-bearing role. The notion of mimicking natural structures in ceramic–metal composites relies primarily on: (i) a segmented layered structure with an optimal ceramic volume fraction (Mayer 2006; Espinosa *et al.* 2009) and (ii) a thin resilient and extensible metallic (nominally non-load-bearing) phase that can act as a ‘lubricant phase’ (Munch *et al.* 2008; Launey *et al.* 2009) to control the degree of sliding between ceramic layers. This controlled sliding provides a very effective source of energy dissipation leading to significant toughening. The concept of the ‘lubricant phase’ has been proven to be very effective in natural composites such as nacre and has been successfully translated to synthetic organic–inorganic composites (Munch *et al.* 2008). However, this does not guarantee that a thin (submicrometre) metallic layer can play the lubricant role needed to recreate this effect in a metal–ceramic structure. A decrease in the metal layer thickness results in higher strength owing to the Orowan-type dislocation strengthening effect (Embury & Hirth 1994), but can also generate brittleness and often poor fracture toughness owing to the increased constraint. This has been clearly observed when the metallic layer thickness is reduced to micrometre size-scale (Was & Foecke 1996; Bloyer *et al.* 1998; Li & Soboyejo 2000). The key question is what will happen when the thickness of the metallic layer is reduced down to the nanoscale. The recent development of nanoscale Cu/Nb-layered composites with extremely fine layer thicknesses down to a few nanometres exhibiting high flow strength of

2.4 GPa and ductility in excess of 25 per cent is very encouraging in this regard and underlines the need for more research in this area (Mara *et al.* 2007, 2008).

## 5. CONCLUSIONS

Using the inspiration of natural materials, we have developed a suite of ceramic–metal hybrid materials with excellent combinations of strength and toughness. We have shown that the concept of ice-templating can be used to process inexpensive laminated ceramic scaffolds with a refined structure over large-scale dimensions. The processing of such ceramic scaffolds infiltrated with higher melting-point metals allows the development of lightweight, strong and tough ceramic-based materials that can operate at elevated temperatures. This has been achieved through careful manipulation of structural architectures to replicate many of the features underlying the unique properties of nacre, in particular its characteristic *R*-curve behaviour which derives from a confluence of toughening mechanisms over multiple length scales. In particular, in this work lamellar  $\text{Al}_2\text{O}_3/\text{Al}$ –Si composites with a 36 vol% ceramic content were processed, and found to display strengths of approximately 300 MPa and fracture toughness values that exceed 40  $\text{MPa}\sqrt{\text{m}}$ . However, we have also shown that a refinement of the microstructure leads to a brittle behaviour owing to a transition from a high-toughness ‘multiple cracking’ fracture mode to a low-toughness ‘single cracking’ mode. We propose that this approach, using the natural design concept of a hard ceramic phase with optimal volume fraction providing for material strength, separated by a softer ‘lubricant’ phase to relieve high stresses in order to enhance toughness, can be successfully used to further develop new structural materials with unprecedented damage-tolerance properties.

This work was supported by the Director, Office of Science, Office of Basic Energy Sciences, Division of Materials Sciences and Engineering, of the US Department of Energy under contract no. DE-AC02-05CH11231. We would like to thank Dr Quentin M. Ramasse at the National Center for Electron Microscopy, which is supported at the Lawrence Berkeley National Laboratory by the Department of Energy under the same contract number, for his help with the scanning transmission electron microscopy, and Dr Mary Laura Lind and Prof. William L. Johnson at the California Institute of Technology for their contact ultrasonic measurements of the elastic moduli.

## REFERENCES

- Aizenberg, J. & Fratzl, P. 2009 Biological and biomimetic materials. *Adv. Mater.* **21**, 387–388. (doi:10.1002/adma.200803699)
- Alman, D. E., Rawers, J. C. & Hawk, J. A. 1995 Microstructural and failure characteristics of metal-intermetallic layered sheet composites. *Metall. Mater. Trans. A* **26**, 589–599. (doi:10.1007/BF02663908)
- Araki, K. & Halloran, J. W. 2004 Room-temperature freeze casting for ceramics with nonaqueous sublimable vehicles in the naphthalene–camphor eutectic system. *J. Am.*

- Ceram. Soc.* **87**, 2014–2019. (doi:10.1111/j.1151-2916.2004.tb06353.x)
- Ashby, M. F., Blunt, F. J. & Bannister, M. 1989 Flow characteristics of highly constrained metal wires. *Acta Metall.* **37**, 1847–1857. (doi:10.1016/0001-6160(89)90069-2)
- Bannister, M. & Ashby, M. F. 1991 The deformation and fracture of constrained metal sheets. *Acta Metall. Mater.* **39**, 2575–2582. (doi:10.1016/0956-7151(91)90072-9)
- Becher, P. F. 1991 Microstructural design of toughened ceramics. *J. Am. Ceram. Soc.* **74**, 255–269. (doi:10.1111/j.1151-2916.1991.tb06872.x)
- Bloyer, D. R., Rao, K. T. V. & Ritchie, R. O. 1998 Fracture toughness and R-curve behavior of laminated brittle-matrix composites. *Metall. Mater. Trans. A* **29**, 2483–2496. (doi:10.1007/s11661-998-0220-0)
- Bonderer, L. J., Studart, A. R. & Gauckler, L. J. 2008 Bioinspired design and assembly of platelet reinforced polymer films. *Science* **319**, 1069–1073. (doi:10.1126/science.1148726)
- Cao, H. C. & Evans, A. G. 1991 On crack extension in ductile/brittle laminates. *Acta Metall. Mater.* **39**, 2997–3005. (doi:10.1016/0956-7151(91)90032-V)
- Cao, H. C., Dalgleish, B. J., Deve, H. E., Elliott, C., Evans, A. G., Mehrabian, R. & Odette, G. R. 1989 A test procedure for characterizing the toughening of brittle intermetallics by ductile reinforcements. *Acta Metall.* **37**, 2969–2977. (doi:10.1016/0001-6160(89)90332-5)
- Chen, L., Ballarini, R., Kahn, H. & Heuer, A. H. 2007 Bioinspired micro-composite structure. *J. Mater. Res.* **22**, 124–131. (doi:10.1557/jmr.2007.0016)
- Clegg, W. J., Kendall, K., Alford, N. M., Button, T. W. & Birchall, J. D. 1990 A simple way to make tough ceramics. *Nature* **347**, 455–457. (doi:10.1038/347455a0)
- Dalgleish, B. J., Lu, M. C. & Evans, A. G. 1988 The strength of ceramics bonded with metals. *Acta Metall.* **36**, 2029–2035. (doi:10.1016/0001-6160(88)90304-5)
- Dalgleish, B. J., Trumble, K. P. & Evans, A. G. 1989 The strength and fracture of alumina bonded with aluminum alloys. *Acta Metall.* **37**, 1923–1931. (doi:10.1016/0001-6160(89)90077-1)
- Deve, H. E. & Maloney, M. J. 1991 On the toughening of intermetallics with ductile fibers: role of interfaces. *Acta Metall. Mater.* **39**, 2275–2284. (doi:10.1016/0956-7151(91)90010-X)
- Deve, H. E., Evans, A. G., Odette, G. R., Mehrabian, R., Emiliani, M. L. & Hecht, R. J. 1990 Ductile reinforcement of  $\gamma$ -TiAl: effects of debonding and ductility. *Acta Metall. Mater.* **38**, 1491–1502. (doi:10.1016/0956-7151(90)90117-Y)
- Deville, S. 2008 Freeze-casting of porous ceramics: a review of current achievements and issues. *Adv. Eng. Mater.* **10**, 155–169. (doi:10.1002/adem.200700270)
- Deville, S., Saiz, E., Nalla, R. K. & Tomsia, A. P. 2006 Freezing as a path to build complex composites. *Science* **311**, 515–518. (doi:10.1126/science.1120937)
- Deville, S., Saiz, E. & Tomsia, A. P. 2007 Ice-templated porous alumina structures. *Acta Mater.* **55**, 1965–1974. (doi:10.1016/j.actamat.2006.11.003)
- E1820–08 2008 *Annual book of ASTM standards, vol. 03.01: metals—mechanical testing; elevated and low-temperature tests; metallography*. West Conshohocken, PA: ASTM International.
- Embury, J. D. & Hirth, J. P. 1994 On dislocation storage and the mechanical response of fine-scale microstructures. *Acta Metall. Mater.* **42**, 2051–2056. (doi:10.1016/0956-7151(94)90030-2)
- Enoki, M., Sakai, K., Kim, B. N. & Kishi, T. 1999 Crack propagation behavior of Ni/NiAl laminate materials. *J. Jpn. Inst. Met.* **63**, 838–843.
- Espinosa, H. D., Rim, J. E., Barthelat, F. & Buehler, M. J. 2009 Merger of structure and material in nacre and bone: perspectives on *de novo* biomimetic materials. *Prog. Mater. Sci.* **54**, 1059–1100. (doi:10.1016/j.pmatsci.2009.05.001)
- Evans, A. G. 1990 Perspective on the development of high-toughness ceramics. *J. Am. Ceram. Soc.* **73**, 187–206. (doi:10.1111/j.1151-2916.1990.tb06493.x)
- Evans, A. G., Suo, Z., Wang, R. Z., Aksay, I. A., He, M. Y. & Hutchinson, J. W. 2001 Model for the robust mechanical behavior of nacre. *J. Mater. Res.* **16**, 2475–2484. (doi:10.1557/JMR.2001.0339)
- Fox, M. R. & Ghosh, A. K. 1999 Structure, strength and fracture resistance of interfaces in NiAl/Mo model laminates. *Mater. Sci. Eng. A* **259**, 261–268. (doi:10.1016/S0921-5093(98)00904-6)
- Fukasawa, T., Ando, M., Ohji, T. & Kanzaki, S. 2001 Synthesis of porous ceramics with complex pore structure by freeze-dry processing. *J. Am. Ceram. Soc.* **84**, 230–232. (doi:10.1111/j.1151-2916.2001.tb00638.x)
- Garcia-Cordovilla, C., Louis, E. & Narciso, J. 1999 Pressure infiltration of packed ceramic particulates by liquid metals. *Acta Mater.* **47**, 4461–4479. (doi:10.1016/S1359-6454(99)00318-3)
- Gaudette, F., Suresh, S., Evans, A. G., Dehm, G. & Rühle, M. 1997 The influence of chromium addition on the toughness of  $\gamma$ -Ni/ $\alpha$ -Al<sub>2</sub>O<sub>3</sub> interfaces. *Acta Mater.* **45**, 3503–3513. (doi:10.1016/S1359-6454(97)00064-5)
- Haggag, F. M. & Underwood, J. H. 1984 Compliance of a 3-point bend specimen at load-line. *Int. J. Fract.* **26**, R63–R65. (doi:10.1007/BF01157556)
- Hartgerink, J. D., Beniash, E. & Stupp, S. I. 2001 Self-assembly and mineralization of peptide-amphiphile nanofibers. *Science* **294**, 1684–1688. (doi:10.1126/science.1063187)
- He, J. L., Wang, J., Li, W. Z. & Li, H. D. 1997 Simulation of nacre with TiN/Pt multilayers and a study of their mechanical properties. *Mater. Sci. Eng. B* **49**, 128–134. (doi:10.1016/S0921-5107(97)00112-8)
- Heathcote, J., Odette, G. R., Lucas, G. E., Rowe, R. G. & Skelly, D. W. 1996 On the micromechanics of low temperature strength and toughness of intermetallic/metallic microlaminate composites. *Acta Mater.* **44**, 4289–4299. (doi:10.1016/1359-6454(96)00112-7)
- Hong, T., Smith, J. R. & Srolovitz, D. J. 1995 Theory of metal–ceramic adhesion. *Acta Metall. Mater.* **43**, 2721–2730. (doi:10.1016/0956-7151(94)00457-S)
- Huang, Y. & Zhang, H. W. 1995 The role of plasticity and interfacial strength in the cracking of metal/ceramic laminates. *Acta Metall. Mater.* **43**, 1523–1530. (doi:10.1016/0956-7151(94)00341-E)
- Huang, Y., Zhang, H. W. & Wu, F. 1994 Multiple cracking in metal-ceramic laminates. *Int. J. Solids Struct.* **31**, 2753–2768. (doi:10.1016/0020-7683(94)90067-1)
- Hwu, K. L. & Derby, B. 1999a Fracture of metal/ceramic laminates—I. Transition from single to multiple cracking. *Acta Mater.* **47**, 529–543. (doi:10.1016/S1359-6454(98)00357-7)
- Hwu, K. L. & Derby, B. 1999b Fracture of metal/ceramic laminates—II. Crack growth resistance and toughness. *Acta Mater.* **47**, 545–563. (doi:10.1016/S1359-6454(98)00358-9)
- Jackson, A. P., Vincent, J. F. V. & Turner, R. M. 1988 The mechanical design of nacre. *Proc. R. Soc. Lond. B* **234**, 415–440. (doi:10.1098/rspb.1988.0056)
- Kamat, S., Su, X., Ballarini, R. & Heuer, A. H. 2000 Structural basis for the fracture toughness of the shell of the conch *Strombus gigas*. *Nature* **405**, 1036–1040. (doi:10.1038/35016535)
- Kaplan, W. D. 1998 The influence of Ca on interface structure and chemistry in melt-infiltrated  $\alpha$ -Al<sub>2</sub>O<sub>3</sub>/Al composites.

- Acta Mater.* **46**, 2369–2379. (doi:10.1016/S1359-6454(98)80018-9)
- Kaplan, W. D., Mullejans, H., Ruhle, M., Rodel, J. & Claussen, N. 1995 Ca segregation to basal surfaces in  $\alpha$ -alumina. *J. Am. Ceram. Soc.* **78**, 2841–2844. (doi:10.1111/j.1151-2916.1995.tb08064.x)
- Kato, T. 2000 Polymer/calcium carbonate layered thin-film composites. *Adv. Mater.* **12**, 1543–1546. (doi:10.1002/1521-4095(200010)12:20<1543::AID-ADMA1543>3.0.CO;2-P)
- Krstic, V. V., Nicholson, P. S. & Hoagland, R. G. 1981 Toughening of glasses by metallic particles. *J. Am. Ceram. Soc.* **64**, 499–504. (doi:10.1111/j.1151-2916.1981.tb10313.x)
- Kruzic, J. J., McNaney, J. M., Cannon, R. M. & Ritchie, R. O. 2004 Effects of plastic constraint on the cyclic and static fatigue behavior of metal/ceramic layered structures. *Mech. Mater.* **36**, 57–72. (doi:10.1016/s0167-6636(03)00031-0)
- Launey, M. E. & Ritchie, R. O. 2009 On the fracture toughness of advanced materials. *Adv. Mater.* **21**, 2103–2110. (doi:10.1002/adma.200803322)
- Launey, M. E., Munch, E., Alsem, D. H., Barth, H. B., Saiz, E., Tomsia, A. P. & Ritchie, R. O. 2009 Designing highly toughened hybrid composites through nature-inspired hierarchical complexity. *Acta Mater.* **57**, 2919–2932. (doi:10.1016/j.actamat.2009.03.003)
- Leichter, H. L. 1966 Impact fracture toughness and other properties of brazed metallic laminates. *J. Spacecr. Rockets* **3**, 1113–1120.
- Lesuer, D. R., Syn, C. K., Sherby, O. D., Wadsworth, J., Lewandowski, J. J. & Hunt, W. H. 1996 Mechanical behaviour of laminated metal composites. *Int. Mater. Rev.* **41**, 169–197.
- Li, M. & Soboyejo, W. O. 2000 An investigation of the effects of ductile-layer thickness on the fracture behavior of nickel aluminide microlaminates. *Metall. Mater. Trans. A* **31**, 1385–1399. (doi:10.1007/s11661-000-0257-1)
- Mara, N. A., Tamayo, T., Sergueeva, A. V., Zhang, X., Misra, A. & Mukherjee, A. K. 2007 The effects of decreasing layer thickness on the high temperature mechanical behavior of Cu/Nb nanoscale multilayers. *Thin Solid Films* **515**, 3241–3245. (doi:10.1016/j.tsf.2006.01.036)
- Mara, N. A., Bhattacharyya, D., Dickerson, P., Hoagland, R. G. & Misra, A. 2008 Deformability of ultrahigh strength 5 nm Cu/Nb nanolayered composites. *Appl. Phys. Lett.* **92**, 231901. (doi:10.1063/1.2938921)
- Mayer, G. 2005 Rigid biological systems as models for synthetic composites. *Science* **310**, 1144–1147. (doi:10.1126/science.1116994)
- Mayer, G. 2006 New classes of tough composite materials: lessons from natural rigid biological systems. *Mater. Sci. Eng. C* **26**, 1261–1268. (doi:10.1016/j.msec.2005.08.031)
- McNaney, J. M., Cannon, R. M. & Ritchie, R. O. 1996 Fracture and fatigue-crack growth along aluminum-alumina interfaces. *Acta Mater.* **44**, 4713–4728. (doi:10.1016/S1359-6454(96)00126-7)
- Mekky, W. & Nicholson, P. S. 2006 The fracture toughness of Ni/Al<sub>2</sub>O<sub>3</sub> laminates by digital image correlation I: experimental crack opening displacement and R-curves. *Eng. Fract. Mech.* **73**, 571–582. (doi:10.1016/j.engfracmech.2005.09.005)
- Meyers, M. A., Chen, P. Y., Lin, A. Y. M. & Seki, Y. 2008a Biological materials: structure and mechanical properties. *Prog. Mater. Sci.* **53**, 1–206. (doi:10.1016/j.pmatsci.007.05.002)
- Meyers, M. A., Lin, A. Y. M., Chen, P. Y. & Muryco, J. 2008b Mechanical strength of abalone nacre: role of the soft organic layer. *J. Mech. Behav. Biomed. Mater.* **1**, 76–85. (doi:10.1016/j.jmbbm.2007.03.001)
- Munch, E., Launey, M. E., Alsem, D. H., Saiz, E., Tomsia, A. P. & Ritchie, R. O. 2008 Tough, bio-inspired hybrid materials. *Science* **322**, 1516–1520. (doi:10.1126/science.1164865)
- Munch, E., Saiz, E., Tomsia, A. P. & Deville, S. 2009 Architectural control of freeze-cast ceramics through additives and templating. *J. Am. Ceram. Soc.* **92**, 1534–1539. (doi:10.1111/j.1551-2916.2009.03087.x)
- Odette, G. R., Chao, B. L., Shekherd, J. W. & Lucas, G. E. 1992 Ductile-phase toughening mechanisms in a TiAl–TiNb laminate composite. *Acta Metall. Mater.* **40**, 2381–2389. (doi:10.1016/0956-7151(92)90157-A)
- Ortiz, C. & Boyce, M. C. 2008 Materials science: bioinspired structural materials. *Science* **319**, 1053–1054. (doi:10.1126/science.1154295)
- Podsiadlo, P. et al. 2007 Ultrastrong and stiff layered polymer nanocomposites. *Science* **318**, 80–83. (doi:10.1126/science.1143176)
- Rao, K. T. V., Soboyejo, W. O. & Ritchie, R. O. 1992 Ductile-phase toughening and fatigue-crack growth in Nb-reinforced molybdenum disilicide intermetallic composites. *Metall. Trans. A* **23**, 2249–2257. (doi:10.1007/BF02646018)
- Rao, K. T. V., Odette, G. R. & Ritchie, R. O. 1994 Ductile-reinforcement toughening in  $\gamma$ -TiAl intermetallic matrix composites: effects on fracture toughness and fatigue-crack propagation resistance. *Acta Metall. Mater.* **42**, 893–911. (doi:10.1016/0956-7151(94)90285-2)
- Rawers, J. & Perry, K. 1996 Crack initiation in laminated metal-intermetallic composites. *J. Mater. Sci.* **31**, 3501–3506. (doi:10.1007/BF00360755)
- Ritchie, R. O. 1988 Mechanisms of fatigue crack-propagation in metals, ceramics and composites: role of crack tip shielding. *Mater. Sci. Eng. A* **103**, 15–28.
- Rohatgi, A., Harach, D. J., Vecchio, K. S. & Harvey, K. P. 2003 Resistance-curve and fracture behavior of Ti–Al<sub>3</sub>Ti metallic–intermetallic laminate (MIL) composites. *Acta Mater.* **51**, 2933–2957. (doi:10.1016/s1359-6454(03)00108-3)
- Rosso, M. 2006 Ceramic and metal matrix composites: routes and properties. *J. Mater. Process. Technol.* **175**, 364–375. (doi:10.1016/j.jmatprotec.2005.04.038)
- Rubner, M. 2003 Materials science: synthetic sea shell. *Nature* **423**, 925–926. (doi:10.1038/423925a)
- Saiz, E. & Tomsia, A. P. 1998 Kinetics of metal-ceramic composite formation by reactive penetration of silicates with molten aluminum. *J. Am. Ceram. Soc.* **81**, 2381–2393. (doi:10.1111/j.1151-2916.1998.tb02634.x)
- Saiz, E., Cannon, R. M. & Tomsia, A. P. 2000 Reactive spreading: adsorption, ridging and compound formation. *Acta Mater.* **48**, 4449–4462. (doi:10.1016/S1359-6454(00)00231-7)
- Saiz, E., Tomsia, A. P. & Sukanuma, K. 2003 Wetting and strength issues at Al/ $\alpha$ -alumina interfaces. *J. Eur. Ceram. Soc.* **23**, 2787–2796. (doi:10.1016/s0955-2219(03)00290-5)
- Sellinger, A., Weiss, P. M., Nguyen, A., Lu, Y. F., Assink, R. A., Gong, W. L. & Brinker, C. J. 1998 Continuous self-assembly of organic–inorganic nanocomposite coatings that mimic nacre. *Nature* **394**, 256–260. (doi:10.1038/28354)
- Shaw, M. C., Marshall, D. B., Dadkhah, M. S. & Evans, A. G. 1993 Cracking and damage mechanisms in ceramic/metal multilayers. *Acta Metall. Mater.* **41**, 3311–3322. (doi:10.1016/0956-7151(93)90060-6)

- Shaw, M. C., Clyne, T. W., Cocks, A. C. F., Fleck, N. A. & Pateras, S. K. 1996 Cracking patterns in metal-ceramic laminates: effects of plasticity. *J. Mech. Phys. Solids* **44**, 801–811. (doi:10.1016/0022-5096(96)00024-5)
- Sigl, L. S., Mataga, P. A., Dalgleish, B. J., McMeeking, R. M. & Evans, A. G. 1988 On the toughness of brittle materials reinforced with a ductile phase. *Acta Metall.* **36**, 945–953. (doi:10.1016/0001-6160(88)90149-6)
- Soboyejo, W. O., Ye, F., Chen, L. C., Bahtishi, N., Schwartz, D. S. & Lederich, R. J. 1996 Effects of reinforcement morphology on the fatigue and fracture behavior of MoSi<sub>2</sub>/Nb composites. *Acta Mater.* **44**, 2027–2041. (doi:10.1016/1359-6454(95)00272-3)
- Tang, Z. Y., Kotov, N. A., Magonov, S. & Ozturk, B. 2003 Nanostructured artificial nacre. *Nat. Mater.* **2**, 413–418. (doi:10.1038/nmat906)
- Trumble, K. P. 1998 Spontaneous infiltration of non-cylindrical porosity: close-packed spheres. *Acta Mater.* **46**, 2363–2367. (doi:10.1016/S1359-6454(98)80017-7)
- Varias, A. G., Suo, Z. & Shih, C. F. 1991 Ductile failure of a constrained metal foil. *J. Mech. Phys. Solids* **39**, 963–986. (doi:10.1016/0022-5096(91)90014-F)
- Wang, R. Z., Suo, Z., Evans, A. G., Yao, N. & Aksay, I. A. 2001 Deformation mechanisms in nacre. *J. Mater. Res.* **16**, 2485–2493. (doi:10.1557/JMR.2001.0340)
- Was, G. S. & Foecke, T. 1996 Deformation and fracture in microlaminates. *Thin Solid Films* **286**, 1–31. (doi:10.1016/S0040-6090(96)08905-5)
- Waschkies, T., Oberacker, R. & Hoffmann, M. J. 2009 Control of lamellae spacing during freeze casting of ceramics using double-side cooling as a novel processing route. *J. Am. Ceram. Soc.* **92**, S79–S84. (doi:10.1111/j.1551-2916.2008.02673.x)
- Wei, H., Ma, N., Shi, F., Wang, Z. Q. & Zhang, X. 2007 Artificial nacre by alternating preparation of layer-by-layer polymer films and CaCO<sub>3</sub> strata. *Chem. Mater.* **19**, 1974–1978. (doi:10.1021/cm062898i)
- Ziegler, T., Neubrand, A., Roy, S., Wanner, A. & Piat, R. 2009 Elastic constants of metal/ceramic composites with lamellar microstructures: finite element modelling and ultrasonic experiments. *Compos. Sci. Technol.* **69**, 620–626. (doi:10.1016/j.compscitech.2008.12.009)